

Optimization of neutrino beams for underground sites in Europe

A. Longhin¹

INFN Laboratori Nazionali di Frascati, via E.Fermi 40, 00044 Frascati, Italy;
on leave from CEA, Irfu, SPP, Centre de Saclay, F-91191 Gif-sur-Yvette, France.

Abstract. We present an optimization procedure for neutrino beams which could be produced at CERN and aimed to a set of seven possible underground sites in Europe with distances ranging from 130 km to 2300 km. Studies on the feasibility of a next generation very massive neutrino observatory have been performed for these sites in the context of the first phase of the LAGUNA design study. We consider specific scenarios for the proton driver (a high power proton driver at 4.5 GeV for the shortest baseline and a 50 GeV machine for longer baselines) and the far detector (a Water Cherenkov for the shortest baseline and a LAr TPC for longer baselines). The flux simulation profits of a full GEANT4 simulation. The optimization has been performed before the recent results on ν_e appearance by reactor and accelerator experiments and hence it is based on the maximization of the sensitivity on $\sin^2 2\theta_{13}$. Nevertheless the optimized fluxes have been widely used since their publication on the internet (2010). This work is therefore mainly intended as a documentation of the adopted method and at the same time as an intermediate step towards future studies which will put the emphasis on the performances of beams for the study of δ_{CP} .

PACS. 14.60.Pq Neutrino mass and mixing

1 Introduction

The feasibility of a European next-generation very massive neutrino observatory in seven potential candidate sites located at distances from CERN ranging from 130 km to 2300 km, has been explored within the LAGUNA¹ design study [1]. In order of increasing distance from Geneva the considered sites have been Fréjus (France) at 130 km, Canfranc (Spain) at 630 km, Caso (Italy) at 665 km, Sierozowice (Poland) at 950 km, Boulby (United Kingdom) at 1050 km, Slănic (Romania) at 1570 km and Pyhäsalmi (Finland) at 2300 km.

When coupled to very intense neutrino beams from CERN, large detectors hosted in such an underground site, could measure with high precision the mixing angle θ_{13} , and eventually determine the neutrino mass hierarchy and the existence of CP violation in the leptonic sector.

The oscillation probability of the $\nu_\mu \rightarrow \nu_e$ channel is shown as a function of the neutrino energy in Fig. 1 for the considered baselines. The energy of the first oscillation maximum spans a wide range of energies for the considered baselines ranging from 0.26 MeV at 130 km up to 4.65 GeV at 2300 km, the full sequence being $\{0.26, 1.27, 1.34, 1.92, 2.12, 3.18, 4.65\}$ GeV.

This parameter is crucial for the optimization of the energy spectrum of the neutrino beam as it will be shown later. Neutrino spectra should cover the region where the oscillation effect is maximal with high statistics and low

intrinsic contamination of ν_e . The study of CP-violation requires to measure the oscillation probability as a function of the neutrino energy, or alternatively to compare large samples of ν_e and $\bar{\nu}_e$ CC events, and suffers in general from neutrino oscillation parameters degeneracies. The possibility to have a broad beam covering the second oscillation maximum at lower energy is beneficial since it provides additional input useful to constraint the effects of mass hierarchy and the δ_{CP} phase [2] and limits the impact of systematic errors on flux normalization by providing spectral information.

In this work we investigate two options for the proton driver: a high power superconducting proton linac at 4.5 GeV and a high power synchrotron at 50 GeV. Concerning the detector technology we consider a 440 kt Water Cherenkov for the 130 km baseline and the low energy proton driver and a 100 kt LAr Time Projection Chamber (LArTPC) at longer baselines with the high energy accelerator. Realistic designs have been proposed for these two detectors: the MEMPHYS [3] and the GLACIER [4] concepts. Previous studies on a high-energy super-beam [5] and a low energy super-beam [7], [8], [9] [6] are available. The simulation of fluxes is based on the GEANT4 [10] libraries and the optimization is performed separately for each one of the considered baselines. The guiding line of the optimization is the final achievable sensitivity on $\sin^2 2\theta_{13}$. Furthermore a direct comparison of a high-energy and low-energy super-beam based on different accelerator scenarios has been done using of a coherent set of simulation tools.

¹ “Large Apparatus studying Grand Unification and Neutrino Astrophysics”, FP7 EU program

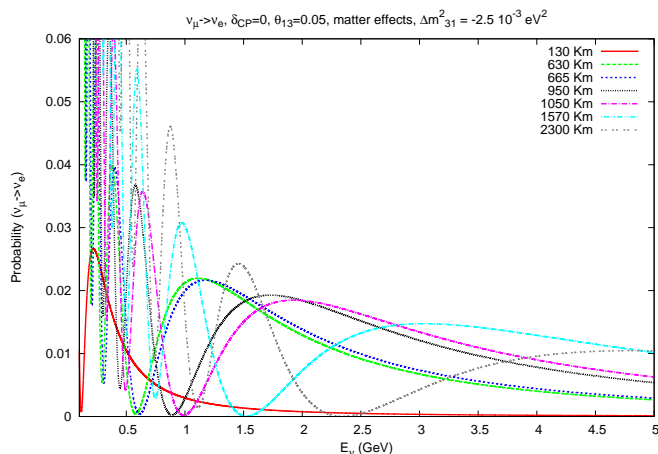


Fig. 1. The neutrino oscillation probability $\mathcal{P}(\nu_\mu \rightarrow \nu_e)$ for the LAGUNA baselines. We assume the inverted hierarchy with $\sin^2 2\theta_{13}=0.05$, $\delta_{CP}=0$ and the presence of matter effects.

2 Proton drivers and detectors

Neutrino rates in conventional beams are at first approximation proportional to the incident primary proton beam power, hence intense neutrino beams can be obtained by trading proton beam intensity with proton energy. So two basic approaches may be considered: a relatively low proton energy accompanied by high proton intensity or a higher proton energy with lower beam current.

In low energy neutrino beams the bulk of ν_e contamination comes from the $\pi \rightarrow \mu$ decay chain and only marginally from kaon decays ($\sim 10\%$ of the ν_e at 4.5 GeV proton energy). This source of background can therefore be more easily constrained due to the correlation with the dominant ν_μ flux component from direct pion decays. In addition, the horn and decay tunnel can be kept at relatively small scales. Finally in the sub-GeV region most of neutrino interactions are quasi-elastic. This final state allows an easy configuration for the calculation of the parent neutrino energy and can be cleanly reconstructed also in a water Cherenkov detector. The π^0 rejection from neutral current events also benefits from the low energy regime since photons are less collinear and energetic allowing the Cherenkov ring patterns generated by e^+e^- to be more resolvable. In order to fulfill the condition of being on the first maximum of oscillation the baseline has to be conformingly small and this offers the advantage of having a small suppression of the flux ($\sim L^{-2}$). Furthermore the determination of CP violation at small baselines is cleaner since there is almost no interplay with CP violating effects related to matter effects.

On the other hand high energy super beams associated to large baselines offer the possibility to study the neutrino mass hierarchy via the study of matter effects in the earth. The neutrino cross section scales about linearly with the energy allowing comparatively larger interaction rates at fixed flux. At high energy neutrino cross sections are free from the large theoretical uncertainties present in the low energy regime (nuclear effects, Fermi motion)

which make the use of near detector compulsory for low energy super-beams. These effects also spoil the neutrino energy resolution. Furthermore the pion focusing is more efficient at high energy of the incident protons due to the more favourable Lorentz boost. We note finally that the chance to measure both first and second maxima increases with the baseline since, in general, the second maximum tends to fall at low energy where resolution and efficiency degrade.

In the following we describe the assumptions for the proton drivers:

- A conceptual design report (CDR2) exists for the high power super conducting linac (HP-SPL) [13]. It is foreseen as a 4 MW machine working at 5 GeV proton kinetic energy. At a first stage it would feed protons to a fixed target experiment to produce an intense low energy (~ 400 MeV) super-beam. On a long time scale this machine could also be used to provide protons for the muon production in the context of a Neutrino Factory.
- The scenario for a high-power 50 GeV synchrotron (HP-PS2) has been initially proposed and discussed in [5]. A factor four in intensity is assumed compared to the baseline parameters defined by the PS2 working group [12] ($1.2 \cdot 10^{14}$ protons with a cycle of 2.4 s). A value of $3 \cdot 10^{21}$ protons on target (p.o.t.) per year could be achieved by doubling both the proton intensity and the repetition rate.

Parameter	HP-SPL	HP-PS2
p kin. energy (GeV)	5	50
repetition frequency (Hz)	50	0.83
p per pulse (10^{14})	1.12	2.5
average power in 10^7 s (MW)	4	2.4
p.o.t./year (10^{21})	56	3

Table 1. Parameters of considered proton drivers.

A summary of the assumed accelerator parameters is given in Tab. 1. For the far detector we concentrated on two designs:

- The MEMPHYS water Cherenkov detector is envisaged as consisting of 3 separate tanks of 65 m in diameter and 65 m height each (440 kt). Such dimensions meet the requirements of light attenuation length in (pure) water and hydrostatic pressure on the bottom PMTs. A detector coverage of 30% can be obtained with about 81.000 PMT of 30 cm diameter per tank. Based on the extensive experience of Super-Kamiokande, this technology is best suited for single Cherenkov ring events typically occurring at energies below 1 GeV.
- GLACIER is a scalable concept for single volume very large LAr TPC with a mass of 100 kt. The powerful imaging will allow to reconstruct with high efficiency electron events in the GeV range and above, while considerably suppressing the neutral current background mostly consisting of misidentified π^0 s.

3 Optimization of the focusing system

The optimization of the neutrino fluxes for the CERN-Fréjus baseline with a Cherenkov detector and a 4.5 GeV proton driver has been studied extensively in [11] so in the following we will take the optimized fluxes obtained in that work and focus on the optimization of the focusing system for longer baselines assuming a LAr far detector and a 50 GeV proton driver.

The focusing system is based on a pair of parabolic horns which we will denote as horn (upstream) and reflector (downstream) according to the current terminology. This schema is the same which is being used for the NuMI beam. The target is modelled as a 1 m long cylinder of graphite ($\rho = 1.85 \text{ g/cm}^3$) and a radius of 2 mm. Primary interaction in the target were simulated with GEANT4 QGSP hadronic package.

The optimization relies on a parametric model of the horn and reflector profiles. The horn radius as a function of the coordinate along the proton beam, $r(z)$, has been parametrized as shown in the first row of Tab.2 in the three z domains $[0, z_1]$, $[z_1, z_2]$, $[z_2, z_3]$. The model contains eleven shape parameters for each magnetic lens ($a, b, c, d, a', b', c', r, z_1, z_2, z_3$) which reduce to nine after requiring continuity at the points z_1 and z_2 ($a, b, c, d, c', z_1, z_2, z_3$). The layout of a typical configuration is shown in Fig. 2.

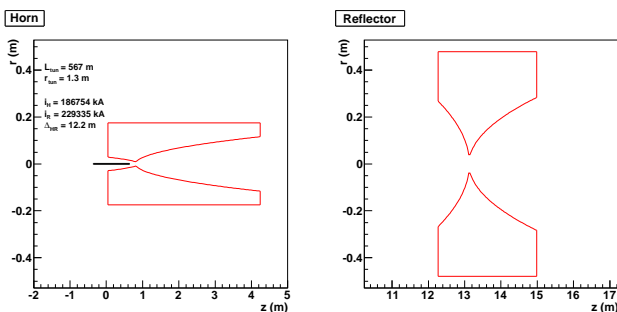


Fig. 2. Layout of the horn/reflector.

In addition to the parameters related to the shape of the horn and the reflector, additional degrees of freedom are: the distance between the horn and reflector (Δ_{HR}), the length and radius of the decay tunnel (L_{tun}, r_{tun}), the longitudinal position of the target (z_{tar}) and the currents circulating in the horn and the reflector (i_H, i_R).

Following the approach already used in [11] for the optimization of the SPL-Fréjus Super Beam, we introduce, as a figure of merit of the focusing, a quantity λ defined as the δ_{CP} -averaged 99 % C.L. sensitivity limit on $\sin^2(2\theta_{13})$ ($:=\lambda_{99}(\delta_{CP})$) in 10^{-3} units

$$\lambda = \frac{10^3}{2\pi} \int_0^{2\pi} \lambda_{99}(\delta_{CP}) d\delta_{CP} \quad (1)$$

In the following we will denote the quantity λ evaluated for a specific baseline L as λ_L . A sample of 10^5 secondary

meson tracks per configuration was used. Fluxes were calculated with 20 energy bins from 0 to 10 GeV. The statistical fluctuations introduced by the size of the sample have been estimated by repeating the simulation for the same configuration several times with independent initialization of the GEANT4 random number engine. The spread is enhanced by the presence of single events which can be assigned large weights. The spread on the parameters λ_L is of the order of 3-4%. The sensitivity limit was calculated with the GLOBES software[15] fixing a null value for θ_{13} and fitting the simulated data with finite values of $\sin^2 2\theta_{13}$ and δ_{CP} sampled in a grid of 10×200 points in the $(\delta_{CP}, \sin^2 2\theta_{13})$ plane for $\delta_{CP} \in [0, 2\pi]$ and $\sin^2 2\theta_{13} \in [10^{-2}, 10^{-4}]$. The 99% C.L. limit was set at the values corresponding to a $\Delta\chi^2$ of 9.21 (2 d.o.f.). The normal hierarchy was assumed in the calculation. We assume running periods of 2 years in ν mode and 8 years in $\bar{\nu}$ mode. The detector response is described in GLOBES by assigning values for the energy resolution, efficiency and defining the considered channels. The parametrization of the MEMPHYS detector is the same which was used in [9]. The event selection and particle identification are the Super-Kamiokande algorithms results. Migration matrices for the neutrino energy reconstruction are used to properly handle Fermi motion smearing and the non-QE event contamination. The reconstructed energy is divided into 100 MeV bins while the true neutrino energy in 40 MeV bins from 0 to 1.6 GeV. Four migration matrices for $\nu_e, \nu_\mu, \bar{\nu}_e$ and $\bar{\nu}_\mu$ are applied to signal events as well as backgrounds. The considered backgrounds are ν_μ^{CC} interactions misidentified as ν_e^{CC} , neutral current events and $\nu_e + \bar{\nu}_e$ intrinsic components of the beam.

In the simulation of the GLACIER detector the considered backgrounds are the intrinsic ν_e and $\bar{\nu}_e$ components in the beam. Reconstructed neutrino energy was divided in 100 MeV bins from 0 to 10 GeV. A constant energy resolution of 1 % is assumed for the signal and the background.

We followed two strategies in the optimization procedure which we will describe in the following subsections.

$r(z)$	$\sqrt{\frac{a-z}{b}} - c$	d	$\sqrt{\frac{z-a'}{b'}} - c'$		
z range	$[0, z_1]$	$[z_1, z_2]$	$[z_2, z_3]$		
Par.	horn	refl.	Par.	horn	refl.
a	85.7	100	d	0.9	3.9
b	7.0	0.135	r	15	40
c	0.2	0.3	z_1	80	97.6
a'	82.2	100.	z_2	83.0	104.8
b'	2.18	0.272	z_3	300	300
c'	0.2	0.3			

Table 2. Analytic parametrization of the horn/reflector radial profile $r(z)$ and central values of the parameters expressed in cm. r is the conductor outer radius.

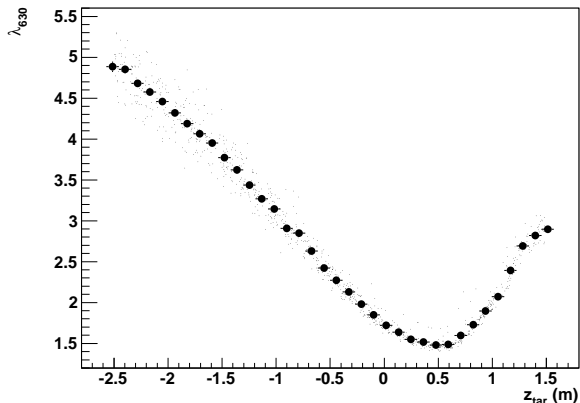


Fig. 3. Dependence of λ_{630} on z_{tar} for the fixed horn search.

3.1 Fixed horn search

In a first step we decided to fix the horn and reflector shapes (central values of Tab. 2), the tunnel geometry ($L_{tun} = 300$ m, $r_{tun} = 1.5$ m) and the circulating currents (200 kA). We then varied the relative positions of the horn, the reflector and the target. We define the distance between the center of the target and the most upstream point of the horn as z_{tar} while we indicate with Δ_{HR} the horn-reflector distance. After having chosen the best point in this space we did a similar exercise in the decay tunnel parameter space (L_{tun} , r_{tun}). At first order these two couples of parameters are expected to be weakly correlated so that doing the optimization in one pair of variables after fixing a specific choice for the other pair should not have a big impact on the final result.

The variables (Δ_{HR} , z_{tar}) were sampled uniformly in the intervals $[0, 300]$ m and $[-1.5, 2.5]$ m respectively. Optimal values were then chosen for each baseline. In general a marked dependence of λ on the longitudinal position of the target (z_{tar}) is observed while variations of Δ_{HR} have a reduced impact. In Fig 3 we show, taking the baseline of 630 km as an example, the dependence of λ_{630} on z_{tar} after marginalizing on Δ_{HR} . For the 630 km baseline the optimal z_{tar} lies around +0.5 m, while for Δ_{HR} a value of 50 m was chosen. At this stage of the optimization the best values for λ_{630} cluster between 1.4-1.5. The first two columns of Tab. 3.1 give the Δ_{HR} and z_{tar} pairs providing the best limit for each baseline (λ_{min} , 3rd column).

After having fixed Δ_{HR} , z_{tar} to the optimal values of Tab. 3.1, the tunnel length L_{tun} , previously fixed at 300 m, was sampled uniformly between $[10, 500]$ m keeping r_{tun} fixed at 1.5 m. The optimized values for L_{tun} are given in Tab. 3.1 (4th column). In the case of $L = 630$ km a gain of order 20% is visible in Fig. 4 (left) decreasing L_{tun} from a 300 to 75 m.

The r_{tun} was then sampled in $[0, 3]$ m having fixed the optimal tunnel length. The right plot of Fig. 4 shows that an improvement is obtained increasing r_{tun} to 2 m. The optimized values for r_{tun} are shown in Tab. 3.1 (5th column). The values of λ obtained after the tunnel optimiza-

tion (λ'_{min}) are shown in the 6th column of Tab. 3.1. The variation between λ_{min} and λ'_{min} shows that the tunnel optimization is particularly effective for the short baselines for which the initial geometry was not appropriate.

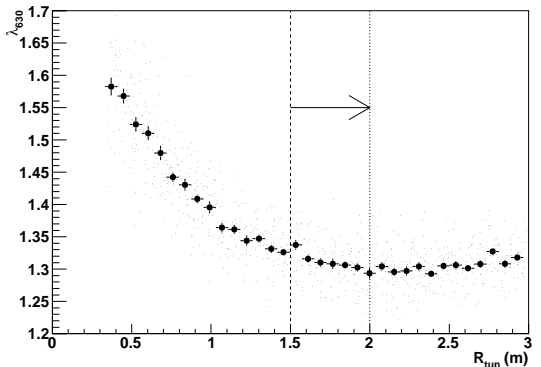
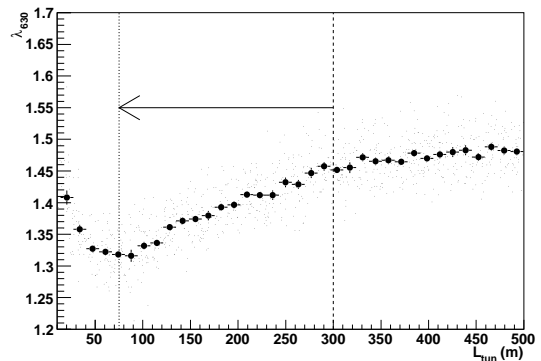


Fig. 4. Dependence of λ_{630} on L_{tun} and r_{tun} in the fixed horn search.

3.2 General search

In order to understand how limiting is the choice of fixing the shape of the conductors and the circulating currents we performed a high statistics general scan of the configurations allowing also these parameters to vary. Also the parameters which were previously optimized were varied since in general changing the shape of the conductors and the currents we do not expect the same optimization to be valid any more.

The shape parameters of the horn and the reflector were sampled with uniform distribution within 50 % of their central values given in Tab. 2. The other parameters were sampled with uniform distribution in the ranges of Tab. 4. The inclusive distributions of the input parameters were compared to the corresponding ones for the subsample with $\lambda < 1.5$ in order to pin down the variables which are effective in producing good results. Despite the smearing effect introduced by the simultaneous variation of many correlated variables, a visible trend is observed

L (km)	z_{tar}^{opt} (m)	Δ_{HR}^{opt} (m)	λ_{min}	L_{tun}^{opt} (m)	r_{tun}^{opt} (m)	λ'_{min}
630	0.5	50	1.4-1.5	75	2	1.3
665	0.45	55	1.4-1.5	90	2.2	1.3
950	0	75	1.3	110	2	1.2
1050	-0.25	4	1.3	200	1	1.3
1570	-0.3	4	1.2-1.3	280	1	1.2
2300	-0.8	4	1.7	400	1.5	1.6

Table 3. Fixed horn shape search. Optimal values for Δ_{HR} , z_{tar} , L_{tun} and r_{tun} .

Parameter	interval	Parameter	Interval
L_{tun}	[200,1000] m	r_{tar}	2 mm
r_{tun}	[0.8,2] m	Δ_{HR}	[4,300] m
z_{tar}	[-2.5, 1.5] m	i_H, i_R	[150,300] kA

Table 4. Focusing system parameters not related to the horn-reflector shapes.

for z_{tar} which exhibits a strong correlation with λ . It is clear that putting the target more and more upstream with respect to the horn, is mandatory to get good exclusion limits, as far as the baseline increases.

The correlation between the longitudinal position of the target with respect to the horn and the mean energy of the ν_μ spectrum ($\langle E_{\nu_\mu} \rangle$) is shown in Fig. 5. Putting the target upstream, high energy pions, which are typically produced at small angles, are preferentially focused resulting in a high energy neutrino spectrum.

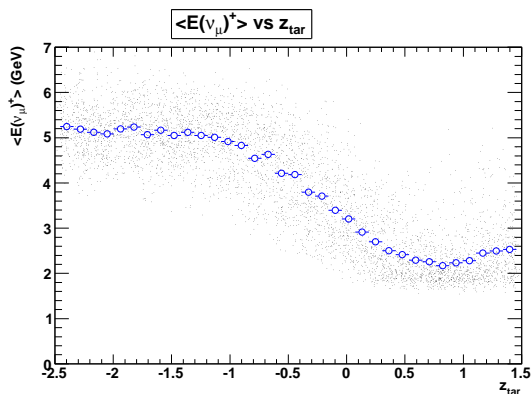


Fig. 5. Correlation between the longitudinal position of the target with respect to the horn and $\langle E_{\nu_\mu} \rangle$.

The correlation between $\langle E_{\nu_\mu} \rangle$ and λ is shown in Fig. 6. In general the optimal energies tend to roughly follow the position of the first oscillation maximum (red vertical lines in the plots). Mean energies below 2 GeV are difficult to get with a 50 GeV proton beam. A possible solution, which has not been considered in this work, could be to go towards an off axis beam for baselines lower than 600 km. The horizontal blue lines show the lowest values for λ obtained with the previous fixed horn shape search.

The achieved performance is not drastically improved by the general search though some gain appears for $L >$

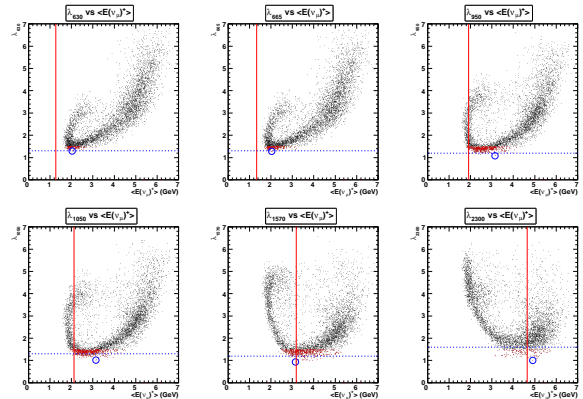


Fig. 6. Correlation between the figure of merit λ and $\langle E_{\nu_\mu} \rangle$ (positive focusing).

1000 km. Blue markers highlight the configuration providing the best limit for each baseline. It turns out that the same configuration provides the best limit both for 630 and 665 km and the same happens for 950-1050 and 1570 km. Given the limited improvement, we decided to stick with the best candidates obtained with the fixed horn shape search. This choice is also motivated by the fact that choosing the configurations with the minimum λ has the disadvantage of being sensitive to statistical fluctuations.

4 Optimized fluxes

The ν_μ fluxes obtained with the optimized focusing setups according to the fixed shape search are shown in Fig. 7 at a reference distance of 100 km. Fluxes are publicly available on the internet [14]. The flux increase as the mean energy increases can be intuitively explained considering that high energy pions are easier to focus since they naturally tend to emerge from the target in the forward direction and the neutrinos they produce have a higher chance to be in the far detector solid angle also thanks to the effect of the Lorentz boost. Un-oscillated interaction rates are given in Tab. 5. It can be noted that considerable samples of τ events becomes collectable with the fluxes optimized for the longer baselines.

5 Conclusions

As it was shown in [6], using the fluxes optimized with the procedure described above, the “discovery potential”

(km)	ν run				$\bar{\nu}$ run			
	ν_μ	ν_e	ν_τ	$\frac{\nu_e+\nu_e}{\nu_\mu+\nu_\mu}$ (%)	$\bar{\nu}_\mu$	$\bar{\nu}_e$	$\bar{\nu}_\tau$	$\frac{\bar{\nu}_e+\bar{\nu}_e}{\bar{\nu}_\mu+\bar{\nu}_\mu}$ (%)
130	41316	174	/	0.42	5915	15	/	0.42
630	36844	486	28	1.5	13652	157	11	2.0
665	38815	516	28	1.5	14287	158	11	2.0
950	37844	349	40	1.0	14700	107	15	1.3
1050	51787	314	148	0.64	21728	88	65	0.60
1570	26785	174	170	0.67	11184	47	73	0.57
2300	17257	110	377	0.67	7577	32	172	0.60

Table 5. Charged current event rates with the optimized fluxes. Fractions are expressed as a percentage. Numbers are normalized to a detector mass of 100 kt and a running time of one year corresponding to $3 \cdot 10^{21}$ p.o.t. for the 50 GeV proton driver and $56 \cdot 10^{21}$ p.o.t. for the 4.5 GeV option.

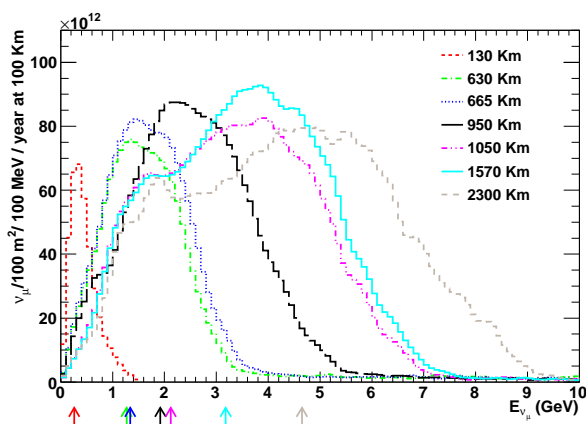


Fig. 7. Neutrino fluxes at 100 km for the systems optimized with the fixed horn shape search. The energies of the oscillation maximum for each baseline (Fig. 1) are indicated with vertical lines having the same color as the corresponding spectrum. The integral fluxes in units of $10^{15} \nu_\mu/100 \text{ m}^2/\text{year}$ are 0.38, 1.59, 1.81, 2.69, 3.56, 3.93 and 4.48 in order of increasing baseline.

for θ_{13} turned out to be, at first order, almost independent of the baseline. Performances of high- and low-energy super-beams are comparable if we assume for both a 5% systematic error on the fluxes. Concerning the high-energy super beam, better results are obtained for intermediate baselines from 950 to 1570 km even though the difference is not marked. This merit factor, despite being obsolete after the recent experimental results, is probably still a reasonable indicator of the precision with which θ_{13} could be measured with these configurations.

This result could be achieved by a systematic tuning of a few basic parameters of the focusing system: the horn-reflector distance, the target position and decay tunnel geometry.

An exhaustive discussion of the physics potential in terms of CP violation and mass hierarchy obtainable with the fluxes whose optimization is described in this work, has been recently developed in [16], [17], [18], [19] and [20].

By adopting a suitable re-definition of the figure of merit, the approach followed in this study could in the future be specialised to the need for optimal sensitivity

on the CP violating effects under the light of the recent measurement of θ_{13} .

6 Acknowledgements

I would like to thank M. Zito for scientific advice and reading of this manuscript and A. Meregaglia for kindly providing the original GLoBES description of the LAr detector. I acknowledge the support from the European Union under the European Commission Framework Programme 07 Design Study EUROnu.

References

1. See <http://www.laguna-science.eu/>.
2. T. Hasegawa, hep-ex/1001.0452.
3. A. De Bellefon *et al.*, hep-ex/0607026.
4. A. Rubbia, hep-ph/0402110.
5. A. Rubbia, hep-ph/1003.1921v1.
6. A. Longhin. PoS, ICHEP2010:325, 2010.
7. M. Mezzetto J. Phys. **G29** (2003), 1781-1784, hep-ex/0302005.
8. J.E. Campagne *et al.* Eur. Phys. J. C **45** (2006).
9. J.E. Campagne *et al.* (2006), hep-ph/0603172.
10. **A 506** (2003) 250-303 IEEE TNS 53 No. 1 (2006) 270-278.
11. A. Longhin, Eur. Phys. J. C **71**:1745, 2011. arXiv:1106.1096v1 [physics.acc-ph].
12. PS2 working group. <https://paf-ps2.web.cern.ch>
13. M. Baylac *et al.*, CERN-2006-006.
14. <http://irfu.cea.fr/en/Phoce/Pisp/index.php?id=72>
15. P. Huber *et al.* Comput. Phys. Commun. 167, 195 (2005), hep-ph/0407333.
16. P. Coloma *et al.* hep-ph/1110.1402.
17. S. K. Agarwalla *et al.* hep-ph/1109.6526.
18. P. Coloma *et al.* hep-ph/1203.5651.
19. S. K. Agarwalla *et al.* hep-ph/1204.4217.
20. <http://agenda.infn.it/contributionDisplay.py?contribId=23&sessionId=5&confId=4722>